ACS APPLIED ENERGY MATERIALS

Open Access

This article is licensed under CC-BY 4.0

www.acsaem.org

Article

A-Site Engineered High Entropy Perovskite Oxides for Rechargeable Zinc-Air Batteries

Cagla Ozgur,‡ Tuncay Erdil,‡ Uygar Geyikci, Huseyin Inan Cihan, Ilker Yildiz, and Cigdem Toparli*

Cite This: *ACS Appl. Energy Mater.* 2026, 9, 6823−6835

Read Online

ACCESS | Metrics & More | Article Recommendations | Supporting Information

ABSTRACT: High-entropy perovskite oxides (HEPOs) combine the compositional flexibility of perovskite oxides with the structural stability of high-entropy oxides, which enables tunable physicochemical properties and robust electronic structures. These attributes make HEPOs particularly attractive as bifunctional air cathode catalysts for alkaline rechargeable zinc−air batteries (ZABs). In this work, we synthesized a series of HEPOs with different A-site cation compositions, $(LaX)(FeCoCrMnZn)O_3$ (X = Sr, Nd, Ca), referred to as LaSr, LaNd, and LaCa. We effectively tailored the work function and oxygen vacancy concentrations by employing an A-site doping strategy, which significantly impact HEPOs electrocatalytic performance. Among the samples, LaNd displayed the lowest oxygen evolution reaction (OER) overpotential and fastest reaction kinetics, resulting from its reduced work function and enhanced oxygen vacancy density. Both mass and specific activity analyses confirmed LaNd's superior OER performance compared to the other A-site variants. When incorporated as a cathode in ZABs, LaNd also exhibited excellent cycling stability and a prolonged operational lifetime, while maintaining competitive oxygen reduction reaction (ORR) activity, underscoring its capability as a reliable bifunctional catalyst. These findings demonstrate that precise A-site cation tuning, while maintaining a stable crystal structure, allows for controlled electronic structure and oxygen vacancy engineering, offering a practical route to optimize HEPO-based air cathodes and enhance the performance and durability of rechargeable ZABs.

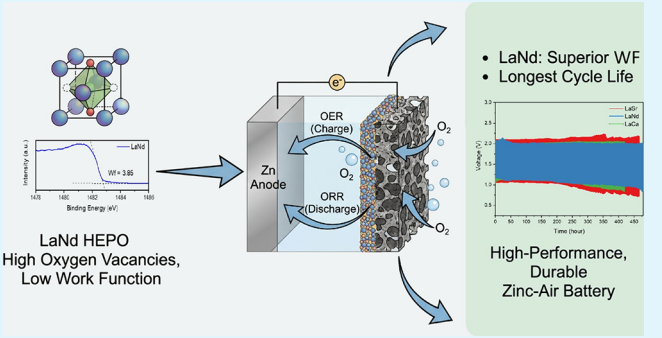

KEYWORDS: *high-entropy perovskite oxides, bifunctional electrocatalysts, zinc-air batteries, oxygen evolution reaction, oxygen reduction reaction, oxygen vacancy, work function, air cathode*

1. INTRODUCTION

Efficient storage of intermittent renewable energy continues to be a major challenge, that makes the development of safe, efficient, and affordable energy storage technologies essential. Among various options, aqueous rechargeable ZABs stand out as a promising and sustainable solution due to their high theoretical energy density, intrinsic safety, and the low cost of zinc.[1−8] These batteries consist of a zinc metal anode, typically an aqueous potassium hydroxide electrolyte, and an air cathode composed of a gas diffusion layer coated with an electrocatalyst. One of the main limitations for aqueous ZABs is the large overpotential at the air cathode that limits the efficiency of operating voltage, hence the overall battery performance. This challenge arises from the sluggish kinetics of the ORR during discharge and the OER during charge, both of which involve complex multi-step mechanisms.[9,10] To ensure the practical applicability of rechargeable ZABs, it is essential to develop cost-effective catalysts that exhibit high efficiency for both ORR and OER while maintaining strong chemical stability. Although platinum-group catalysts such as Pt/C, IrO_2, and RuO_2 are effective and seen as state-of-art electrocatalysts, their scarcity, cost and poor long term stability hinder broad application of ZABs.[11−13] It is clear that development of alternative electrocatalysts has utmost importance for the ZAB applications.[14−19]

The use of transition-metal-based perovskite oxides (ABO_3) as alternatives to Pt-group catalysts has drawn attention, owing to their low cost, straightforward synthesis, and versatile structural and compositional design.[20−22] Defect engineering is a vital strategy for optimizing the electrocatalytic behavior of perovskite oxides, as structural defects can strongly influence charge distribution, spin transitions, and electronic band structures.[23,24] Among these defects, oxygen vacancies are particularly significant and are commonly introduced to enhance catalytic activity. They can be generated through reduction

Received: January 30, 2026
Revised: April 11, 2026
Accepted: May 11, 2026
Published: May 28, 2026

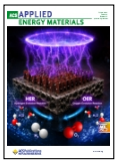

ACS Publications

© 2026 The Authors. Published by American Chemical Society

Downloaded from pubs.acs.org/aaemcq/article-pdf/9/11/6823/6601946/ae-2026-00383e.pdf by ORTA DOGU TEKNIK UNIV user on 23 September 2026

treatments or by deliberately modifying the A-site composition of perovskite oxides. In particular, A-site engineering plays an important role in controlling the overall electronic environment and oxygen vacancy concentration of the lattice.[25] For example, substituting La^{3+} with Sr^{2+} in $LaCoO_3$ strengthens Co 3d−O 2p coupling and increases Co^{4+} content, thereby boosting OER activity.[26] Likewise, introducing A-site deficiency in $LaFeO_3$ facilitates the formation of oxygen vacancies and Fe^{4+} species, which significantly lower the OER overpotential.[27] Another alternative to Pt-group catalysts has emerged as a promising candidate is high entropy oxides (HEOs).[10,28−30] HEOs differ from traditional catalysts by exhibiting multi-element synergy enabled by unsaturated coordination, entropy stabilization, and a variety of active centers, which together accelerate charge transport, facilitate intermediate adsorption and desorption, and extend operational stability.[31,32] Additionally, tunability of HEOs adjusts the electronic structure and oxygen adsorption and desorption balance, have a positive effect on the electrochemical performance. In recent literature, there is a significant amount of increase in the HEO studies for ZAB applications due to those properties. Furthermore, HEOs can be manufactured with various morphologies and crystal structures, including perovskite crystal structure.[33]

HEPOs combine the aforementioned advantages of perovskite oxides and HEOs.[34,35] In a typical HEPO, the A-sites are occupied by rare-earth and alkaline-earth cations, while the B-site sublattice is tailored in a high-entropy configuration by integrating multiple transition metals, effectively enhancing structural complexity and functional tunability. Nguyen et al. synthesized a series of lanthanum-based HEPOs and found that the optimized composition, $La(CrMnFeCo_2Ni)O_3$ (LaB_2Co), exhibited the highest OER activity. This enhanced performance was attributed to the high concentration of oxygen vacancies and the elevated oxidation states of Co and Mn.[36] In our previous study, adjusting B-site cation ratios in HEPOs enhanced their electrocatalytic performance. The $La(Fe_{0.2}Co_{0.3}Mn_{0.1}Cr_{0.2}Zn_{0.2})O_{3-}\delta$ (La5M−Co/Mn) composition, rich in oxygen vacancies, achieved a low OER overpotential and a bifunctional index. As a ZAB cathode, it surpassed the equimolar one in power density, capacity, and cycling stability, showing that cation ratio tuning induces lattice distortion and electronic modulation to boost bifunctional catalytic activity.[17] While previous studies mainly focused on the influence of B-site cations, the A-site cation also affects the crystal structure, thereby modulating the electronic and optical properties. Defect engineering at the A-site further alters the valence states of B-site metal ions, which are regarded as the active sites[37,38] of the perovskite oxides.[39] However, literature lacks a systematic investigation of how these modifications impact OER/ORR activity and ZAB performance. In this work, we produced and evaluated HEPOs with A-site substitutions (A/HEPOs). We designed series of $(LaX)(FeCoCrMnZn)O_3$ with X = Sr, Nd, Ca (LaSr, LaNd, LaCa) HEPOs. Among the A-site modified HEPOs LaNd exhibited the lowest OER overpotential and the fastest reaction kinetics, which can be attributed to its reduced work function and elevated oxygen vacancy concentration. Both mass and specific activity measurements confirmed LaNd's superior OER performance compared to other A-site compositions. When employed as a cathode in Zn−air batteries, LaNd HEPO also demonstrated enhanced cycling stability and prolonged operational lifetime.

2. EXPERIMENTAL SECTION

2.1. Materials Synthesis

$((LaX)(FeCoCrMnZn)O_3$, X = Sr, Nd, Ca) high-entropy perovskite oxides labeled LaSr, LaNd and LaCa were synthesized via a modified Pechini sol−gel route. Stoichiometric amounts, e.g. for LaNd sample 0.5 moles of $La(NO_3)_3{\cdot}6H_2O$ and $Nd(NO_3)_3.6H_2O$, and 0.2 moles of each B-site elements, $Cr(NO_3)_3.9H_2O$, $Mn(NO_3)_2{\cdot}4H_2O$, $Fe(NO_3)_3.9H_2O$, $Co(NO_3)_2{\cdot}6H_2O$, $Zn(NO_3)_2.6H_2O$ were first dissolved in deionized water (18.2 MΩ·cm). Subsequently, acrylamide (AC) and citric acid (CA) were introduced as complexing agents together with the metal cations, maintaining a molar ratio of 1:9:3. The resulting solution was continuously stirred on a hot plate at 100 °C until gel formation occurred. After the water had completely evaporated, the resulting gel was dried at ∼225 °C for 24 h. The A-site modified LaSr, LaNd, and LaCa samples were calcined at 600 °C for 15 h, and all calcined powders were finally annealed at 1000 °C to obtain single-phase materials.

2.2. Materials Characterization

Crystal structures of A/HEPOs were identified by room-temperature powder X-ray diffraction (XRD) using Ni-filtered Cu Kα radiation (λ = 1.5406 Å) over 2θ = 20°−90°. To investigate potential phase changes, XRD analysis was performed again on the samples following the cyclic charge-discharge tests. The spectra were collected directly from the carbon cloth after the long-term test, during which both the substrate and the active electrocatalysts continuously interacted with the electrolyte components (KOH and $Zn(OAc)_2$). Structural refinements were carried out by Rietveld analysis using GSAS/EXPGUI. Surface elemental and chemical-state analyses of the A/HEPOs were performed by X-ray photoelectron spectroscopy (XPS) (PHI 5000 VersaProbe, Al Kα), with spectra calibrated to the C 1s peak at 284.6 eV. Quantitative elemental composition and stoichiometry were verified by Inductively Coupled Plasma − Optical Emission Spectroscopy (ICP-OES). Work function (WF) measurements were performed utilizing the PHI VersaProbe 5000 X-ray Photoelectron Spectroscopy (XPS) system to systematically analyze the surface electronic properties of the investigated samples. The high-energy resolution and surface sensitivity of the instrument enabled accurate determination of the WF values through secondary electron cutoff analysis.

2.3. Electrochemical Performance Measurements

Electrochemical behavior of the LaSr, LaNd, and LaCa A/HEPO samples was evaluated on a rotating disk electrode (RDE) setup with a GAMRY Reference 3000 potentiostat/galvanostat/ZRA. Measurements used a conventional three-electrode cell (Ag/AgCl reference, graphite counter, glassy carbon working electrode (GCE)). Catalyst inks (HEPO powder, Super P carbon, Nafion, ethanol) were drop-cast on the GCE to a loading of 0.15 $mg{\cdot}cm^{-2}$. Tests were carried out in 1 M potassium hydroxide (KOH) pre-saturated with O_2 for 30 min. For OER, electrodes were rotated at 1600 rpm, activated by 10 cyclic voltammetry (CV) cycles, and linear sweep voltammetry (LSVs) were recorded between 0.2 and 1.1 V vs. Ag/AgCl (potentials converted to reversible hydrogen electrode (RHE) via the Nernst equation). Electrochemical impedance spectroscopy (EIS) was performed at 1.641 V vs. RHE with a 10 mV AC perturbation across 10^5−10^2 Hz. Electrochemically active surface area (ECSA) was estimated from double-layer capacitance (C_{dl}) derived from non-faradaic CVs at multiple scan rates. The ECSA was determined by dividing the C_{dl} value by the specific capacitance (Cs), which was taken as 0.040 mF cm^{-2} in 1 M KOH based on literature.[40−42] ORR measurements employed the same workflow but a potential window of 0.2−(−0.8) V vs. Ag/AgCl; LSVs collected at 400–2000 rpm were analyzed with the Koutecky−Levich equation to extract kinetic current densities and electron-transfer numbers. To clarify the contribution of the carbon support, the electrochemical activity of Super P carbon was

Downloaded from pubs.acs.org/aaemcq/article-pdf/9/11/6823/6019466/ae-2026-00383e.pdf by ORTA DOGU TEKNIK UNIV user on 23 September 2026

https://doi.org/10.1021/acsaem.6c00383
ACS Appl. Energy Mater. 2026, 9, 6823−6835

independently evaluated, and the results have been included in the Supporting Information Figure S1.

2.4. Zinc−Air Battery Performance Measurements

ZAB tests used zinc foil anodes and A-site modified HEPO-based air cathodes. The electrolyte was a mixture of 6.0 M KOH and 0.2 M $Zn(OAc)_2$. Cathodes consisted of carbon cloth as a gas-diffusion layer, the HEPO catalyst layer, and a PTFE film to permit O_2 while limiting electrolyte loss. Power density curves were recorded over 0–200 mA·cm^{-2} and charge−discharge polarization characteristics were measured. Full discharge capacities were determined after complete discharge at 5, 10 and 20 mA·cm^{-2}. Rate capability and cycling stability were assessed by comparing voltages under various discharge currents (0–20 mA·cm^{-2}) and then returning to open-circuit. Long-term cycling tests were conducted at a constant 5 mA·cm^{-2} with alternating 5-minute charge and 5-minute discharge periods.

3. RESULTS AND DISCUSSION

3.1. Materials Characterization

Figure 1 shows the Rietveld-refined XRD patterns for the A-site modified HEPO samples LaSr, LaNd and LaCa. The LaSr specimen displays a sharp, single-phase cubic perovskite pattern with no detectable reflections from secondary oxides or hydroxides, indicating excellent phase purity and structural homogeneity. The LaNd composition likewise forms a single perovskite phase, although its lattice is indexed as orthorhombic rather than cubic. By contrast, the LaCa sample exhibits more pronounced secondary reflections and therefore lower phase purity than LaSr and LaNd. Despite the predominance of the perovskite matrix, LaCa shows small additional peaks at roughly 2θ = 25°, 30°, 35° and 50°, consistent with secondary oxide impurities that may partially disrupt the perovskite lattice. These impurity phases introduce microscale heterogeneity that can substantially affect electrochemical response. Consequently, the diminished catalytic activity of LaCa can be attributed to these impurity phases, which highlight the critical role of structural purity and phase stability for achieving target electrochemical performance in HEPOs. Consistency between the synthesized A/HEPO products and their target compositions was verified by ICP-OES, with results summarized in Table 1.

Figure 2 shows the O 1s XPS core-level spectra for the LaSr, LaCa and LaNd samples. The O 1s envelopes can be deconvoluted into four characteristic components. The first two peaks correspond to oxygen species involved in lattice bonding. The first peak, observed at approximately ∼528.5 eV binding energy, represents lattice oxygen (i.e., the presence of O^{2-} ions in the lattice). This is followed by a peak near ∼529 eV, which is attributed to more oxidative oxygen species and is associated with O_2^{2-}/O^- (peroxide/superoxide) configurations. The subsequent pair of peaks reflect surface/adsorbed species related to oxygen vacancies. The peak around∼531 eV is assigned to OH^- or O_2-related species and is particularly relevant for OER and ORR. OH^- species interact with active metal centers during OER to facilitate the formation of oxyhydroxide phases, which in turn promote O_2 evolution. This peak can also serve as an indica- tor for the relative amount of O_2 produced during OER. In contrast, molecular O_2 is the primary reactant in the ORR, forming the focus of oxygen reduction. Finally, the peak observed at ∼532 eV corresponds to molecular water (H_2O) or surface-bound carbonates (CO_3^{2-}). The O 1s spectra in Figure 2 clearly show that LaNd has the highest relative intensity for the OH^-/O_2 component among the samples studied.

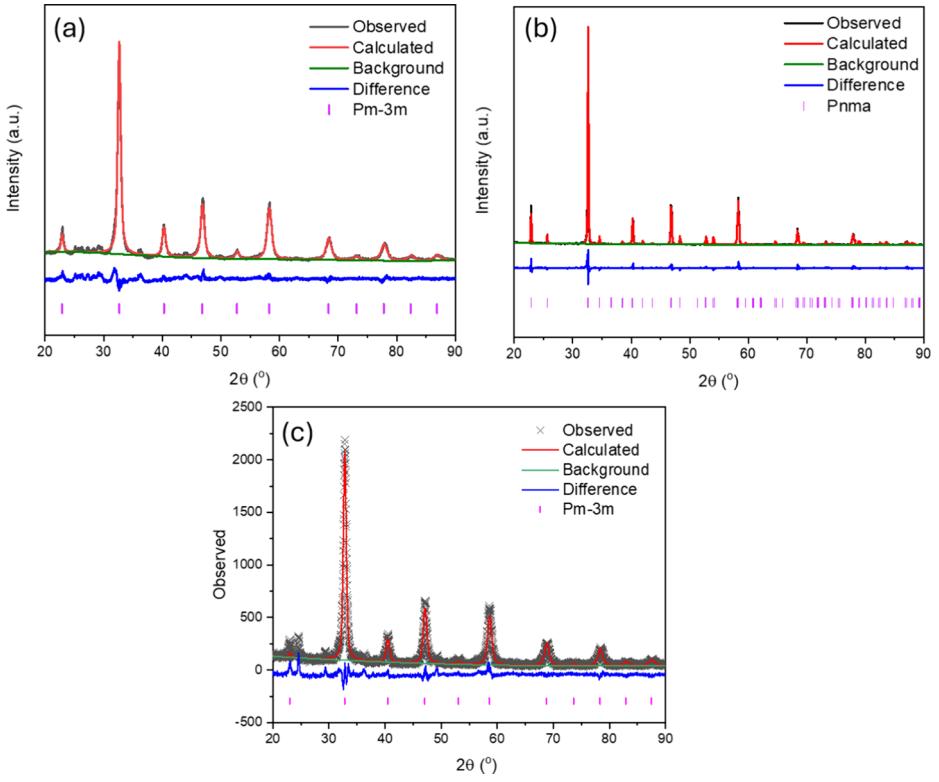

Figure 1. Rietveld analysis graphs of (a) LaSr, (b) LaNd (c) LaCa A/HEPOs.

https://doi.org/10.1021/acsaem.6c00383
ACS Appl. Energy Mater. 2026, 9, 6823−6835

Downloaded from pubs.acs.org/aaemcq/article-pdf/9/11/6823/6601946/ae-2026-00383e.pdf by ORTA DOGU TEKNIK UNIV user on 23 September 2026

Table 1. ICP Analysis of LaSr, LaNd, and LaCa Samples

	LaSr		land		LaCa	
	measured wt %	expected wt %	measured wt %	expected wt %	measured wt %	expected wt %
La	29 ± 1	31.76	28 ± 1	29.12	32 ± 1	35.63
Cr	4.5 ± 0.1	4.76	4.5 ± 0.1	4.21	5.1 ± 0.1	5.34
Mn	4.7 ± 0.1	5.02	4.6 ± 0.1	4.45	5.3 ± 0.1	5.64
Fe	4.5 ± 0.1	5.11	4.4 ± 0.1	4.52	5.4 ± 0.1	5.73
Co	5.0 ± 0.2	5.39	5.0 ± 0.1	4.77	5.8 ± 0.1	6.05
Zn	5.6 ± 0.2	5.98	5.5 ± 0.1	5.29	6.3 ± 0.2	6.71
Sr	16.4 ± 0.4	20.03				
Nd			29 ± 1	29.2		
Ca					10.0 ± 0.1	10.28

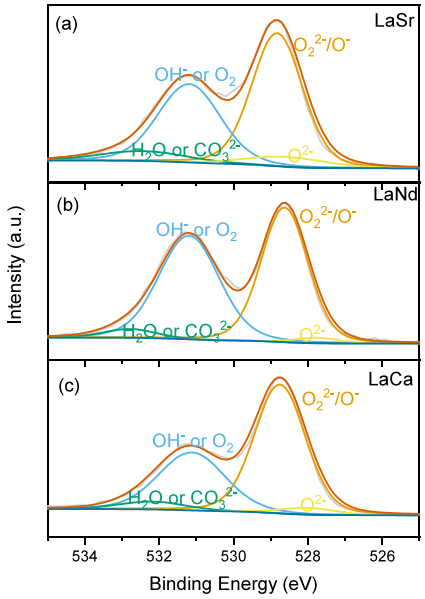

Figure 2. XPS O 1s core-level spectra of (a) LaSr (b) LaNd (c) LaCa A/HEPO samples.

In Figure 3a, the La 3d XPS core level spectra reveal that substituting different A-site cations (Sr, Ca, Nd) does not noticeably alter the oxidation state of La. Consistency across all three spectra confirms that the oxidation environment of La remains stable regardless of the A-site composition. The oxidation state can be deduced from the energy gap between the multiplet-split components of the La $3d_5/_2$ signal,[43] which is measured to be approximately 3.9 eV for each sample, indicating no significant variation among them.

Spectral analyses of the individual A-site elements, such as Sr 3d in LaSr, Ca 2p in LaCa, and Nd 3d in LaNd in the Figures 3b–d, verify that each metal maintains its expected + 2 oxidation state. Additional MCO_3 (M = Sr, Ca) peaks appear, which are attributed to carbonate phases formed when SrO or CaO readily react with atmospheric CO_2.[44]

Figure 4 illustrates the deconvoluted X-ray photoelectron spectroscopy core level spectra for Co 2p, Cr 2p, Fe 2p, Mn 2p, and Zn 2p, in which distinct spectral features were successfully isolated despite the complexity of deconvoluting the Fe 2p region due to the overlapping Co LMM Auger peak. The Co 2p spectra (Figure 4a) and display peaks for Co $2p_{3/2}$ (780 eV), its satellite (786 eV), Co $2p_{1/2}$ (796 eV), and its satellite (802 eV); these strong satellite features indicate that Cobalt exists primarily in the Co^{2+} oxidation state across all HEPO samples. In Figure 4b and the Cr 2p spectra show Cr $2p_{3/2}$ and Cr $2p_{1/2}$ signals at 576.0 and 586 eV, respectively, pointing to a predominant Cr^{3+} state in LaSr, LaNd, and LaCa, although Cr^{6+} was also detected in the LaSr and LaCa samples. Figure 4c highlights the Fe 2p region with peaks at 711 eV (Fe $2p_{3/2}$), 718 eV (satellite), and 724 eV (Fe $2p_{1/2}$), where the presence and unskewed position of the satellite confirm the coexistence of Fe^{3+} and Fe^{2+} valence states in all samples. Additionally, the Mn 2p spectra in Figure 4d exhibit peaks at 641 eV Mn $2p_{3/2}$ and 653 eV (Mn $2p_{1/2}$), with the absence of MnO satellites suggesting the presence of Mn_2O_3 and an Mn^{3+} oxidation state throughout the samples. Finally, the Zn 2p spectra in Figure 4e confirm a consistent Zn^{2+} state across all samples, characterized by Zn $2p_{3/2}$ and Zn $2p_{1/2}$ peaks at binding energies of 1021 and 1045 eV, respectively.

Work-function measurements obtained from the valence-band spectra via XPS (Figure 5) yielded values of 3.85 eV for -LaSr, 4.0 eV for LaCa, and 2.7 eV for -LaNd. The observed WF variations indicate significant differences in surface composition, electronic structure, or applied surface treatments across the samples. These findings provide us important information about the interfacial behavior and overall electronic properties of the materials. As a physical quantity representing the minimum energy required for an electron to escape from the surface to the vacuum level, the work function has a strong influence on electrochemical reaction kinetics. Consequently, a smaller work function correlates with improved OER efficiency.

3.2. Electrochemical Characterization

In rechargeable ZABs, two key electrochemical reactions occur at the air cathode: ORR during discharge and the OER during charge. During the discharge, oxygen from the ambient atmosphere is supplied to the cathode, where it undergoes reduction through the ORR process. When the battery is recharged, these electrochemical pathways are reversed, leading to the evolution of oxygen at the same electrode. Therefore, to explore how A-site doping influences catalytic activity, a series of electrochemical evaluations were performed using A/HEPO-based electrocatalysts. The experiments were conducted in an oxygen-saturated 1 M KOH electrolyte employing a conventional three-electrode configuration. LSV curves were collected, corrected for internal resistance (IR), and normalized to the geometric surface area of the GCE (0.196 cm^2) to ensure accurate comparison of electrochemical performance.

Downloaded from pubs.acs.org/aaemcq/article-pdf/9/11/6823/6019466/ae-2026-00383e.pdf by ORTA DOGU TEKNIK UNIV user on 23 September 2026

https://doi.org/10.1021/acsaem.6c00383
ACS Appl. Energy Mater. 2026, 9, 6823–6835

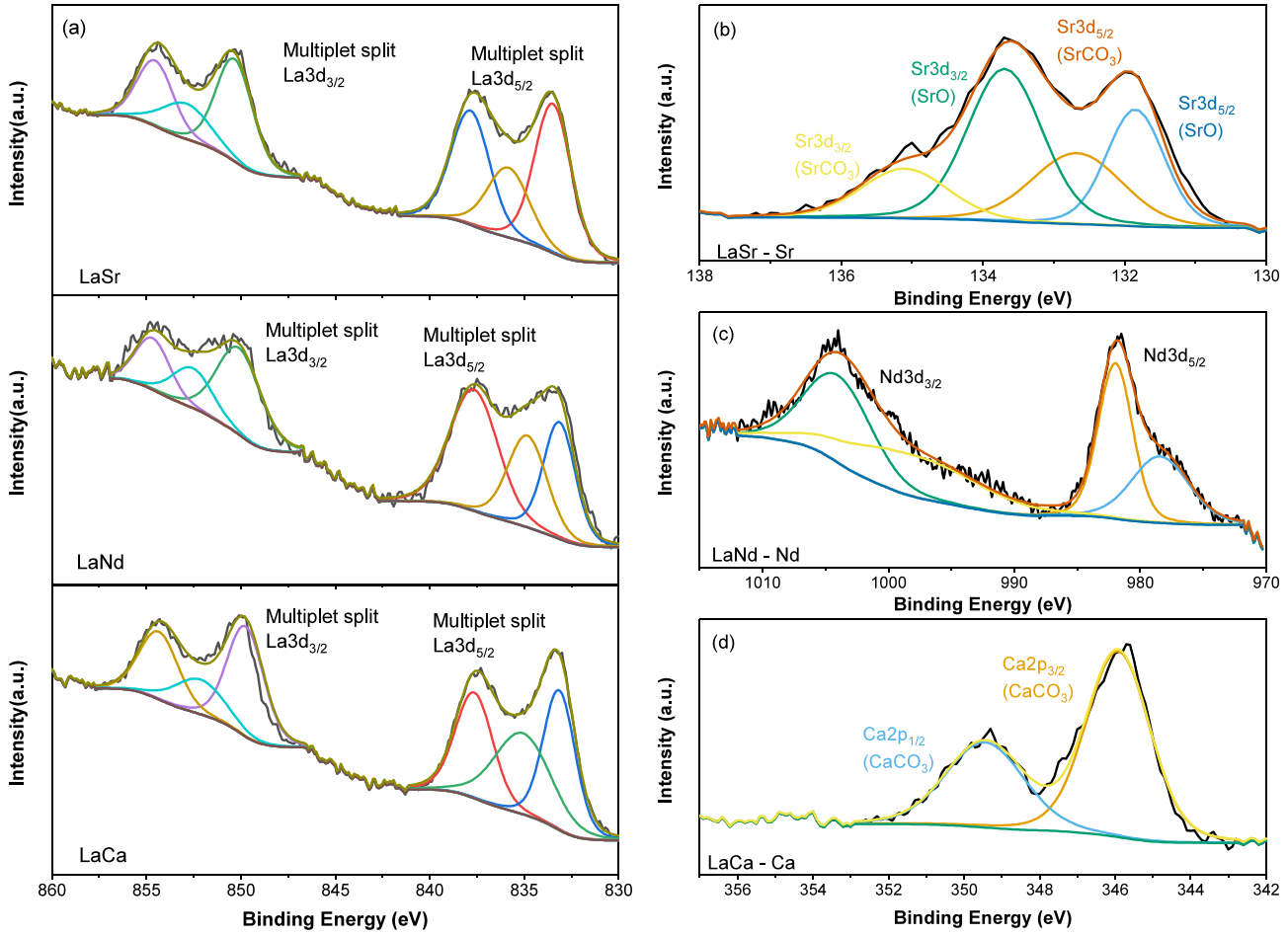

Figure 3. XPS core-level spectra for the A/HEPO samples (a) La 3d spectra of LaSr, LaNd, and LaCa (b) Sr 3d spectrum of LaSr (c) Nd 3d spectrum of LaNd (d) Ca 2p spectrum of LaCa.

LSV results are illustrated in Figure 6a. The overpotential at a current density of 10 mA cm^{-2} was found to be 479 mV for LaSr, 459 mV for LaNd, and 549 mV for LaCa. (Average overpotentials from RDE measurements performed using independently prepared catalyst inks are 486 mV for LaSr, 468 mV for LaNd, and 562 mV for LaCa. See Supporting Information Figure S2). Among these electrocatalysts, LaNd displayed the lowest overpotential, likely due to its reduced work function and higher concentration of oxygen vacancies compared with the other A/HEPO samples.

To further assess the reaction kinetics, Tafel slopes were calculated (Figure 6b), yielding values of 119 mV dec^{-1} for LaSr, 92 mV dec^{-1} for LaNd, and 161 mV dec^{-1} for LaCa. The smaller Tafel slope of LaNd suggests faster electrochemical kinetics relative to LaSr and LaCa. EIS was used to investigate the charge-transfer behavior of the electrocatalysts, with the corresponding Nyquist plots shown in Figure 6c. The measured charge-transfer resistance (R_{ct}) values were 107.1 Ω for LaSr, 94 Ω for LaNd, and 37.8 Ω for LaCa. Although LaCa exhibits the lowest R_{ct} and highest apparent conductivity, XRD indicates secondary oxide phases that may artificially enhance conductivity, making it less reliable. LaNd, with the second-lowest R_{ct} and no detectable secondary phases, provides a more trustworthy measure of intrinsic charge-transfer properties. This more reliable conductivity correlates well with the enhanced OER activity observed for LaNd, supporting its superior intrinsic electrocatalytic performance among the A-site variants.

The ECSA was estimated from the C_{dl}, derived from CV curves recorded at various scan rates in the non-Faradaic region (Figure 6d). The C_{dl} values were 5.10 mF cm^{-2} for LaSr, 1.36 mF cm^{-2} for LaNd, and 4.77 mF cm^{-2} for LaCa, indicating that LaSr has the largest ECSA.

Finally, the intrinsic catalytic activity was evaluated through mass activity (MA) and specific activity (SA) (Figure 6e). To eliminate the effects of mass loading and ECSA on OER activity, the mass loadings and ECSAs of the samples were normalized to the measured OER current density. At an overpotential of 300 mV, both the MA and SA were calculated respectively from the mass loading and ECSA to enable a fair comparison of intrinsic catalytic performance. LaNd exhibited the highest activity, with an MA of 81.33 A g^{-1} and an SA of 0.36 mA cm^{-2}. For LaSr and LaCa, the MA values were 65.53 and 39.40 A g^{-1}, while the SA values were 0.08 and 0.05 mA cm^{-2}, respectively. Notably, the LaSr sample exhibits a significantly higher ECSA compared to the LaNd sample. Despite possessing a lower density of exposed active sites, LaNd demonstrates superior specific activity. This distinction clearly indicates that the catalytic enhancement observed upon Nd incorporation does not stem from an increased active surface area. Rather, the Nd substitution fundamentally improves the

Downloaded from pubs.acs.org/aaemcq/article-pdf/9/11/6823/6019466/ae-2026-00383e.pdf by ORTA DOGU TEKNIK UNIV user on 23 September 2026

https://doi.org/10.1021/acsaem.6c00383
ACS Appl. Energy Mater. 2026, 9, 6823−6835

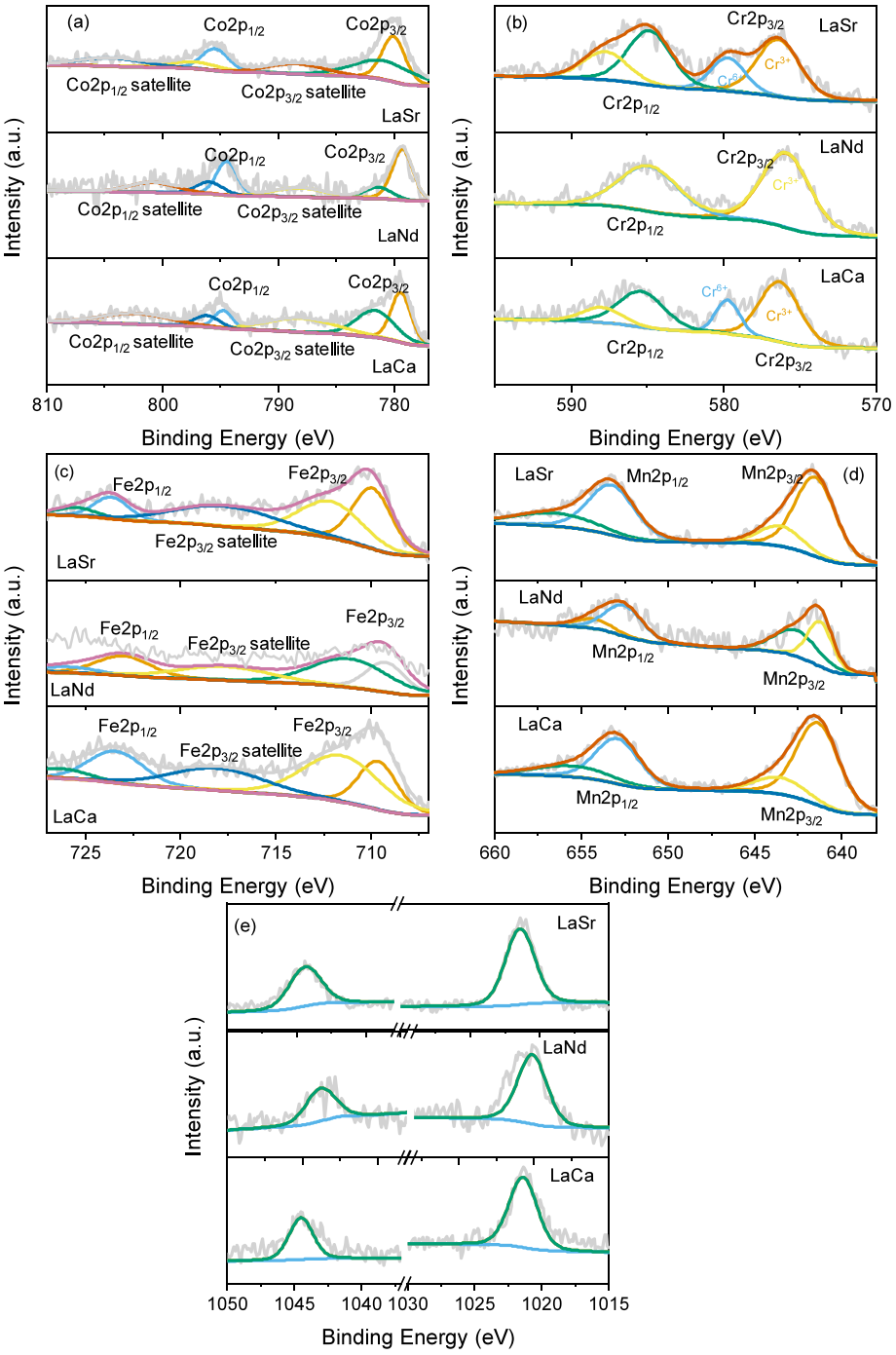

Figure 4. XPS core-level spectra for the A/HEPO samples (a) Co 2p spectra of LaSr, LaNd, and LaCa (b) Cr 2p spectra of LaSr, LaNd, and LaCa (c) Fe 2p spectra of LaSr, LaNd, and LaCa (d) Mn 2p spectra of LaSr, LaNd, and LaCa (e) Zn 2p spectra of LaSr, LaNd, and LaCa.

intrinsic activity of the individual catalytic sites. Therefore, the superior performance of LaNd is intrinsically driven by the optimized active site quality rather than a simple geometric surface area effect.

Figure 7 illustrates the ORR activity of LaSr, LaNd, and LaCa electrocatalysts. The LSV curves in Figure 7a show onset potentials at –1 mA cm^{-2} of 0.84 V for LaSr, 0.66 V for LaNd, and 0.76 V for LaCa. The half-wave potentials were measured as 0.71 V for LaSr, 0.56 V for LaNd, and 0.60 V for LaCa. And the limiting current densities were –8.37, –8.24 and –6.46 mA cm^{-2} for LaSr, LaCa, and LaNd, respectively. It indicates that LaSr exhibits slightly higher ORR activity compared to LaNd and LaCa.

Tafel plots were employed to determine the Tafel slopes (Figure 7b), which were calculated as –219 mV dec^{-1} for LaSr, –89.41 mV dec^{-1} for LaNd, and –238 mV dec^{-1} for LaCa.

The lowest Tafel slope observed for LaNd indicates faster ORR kinetics compared with the other A-site doped HEPO samples.

The Koutecky–Levich (K–L) equation was applied to evaluate the number of electrons transferred and the kinetic current

https://doi.org/10.1021/acsaem.6c00383
ACS Appl. Energy Mater. 2026, 9, 6823–6835

Downloaded from pubs.acs.org/aaemcq/article-pdf/9/11/6823/6601946/ae-2026-00383e.pdf by ORTA DOGU TEKNIK UNIV user on 23 September 2026

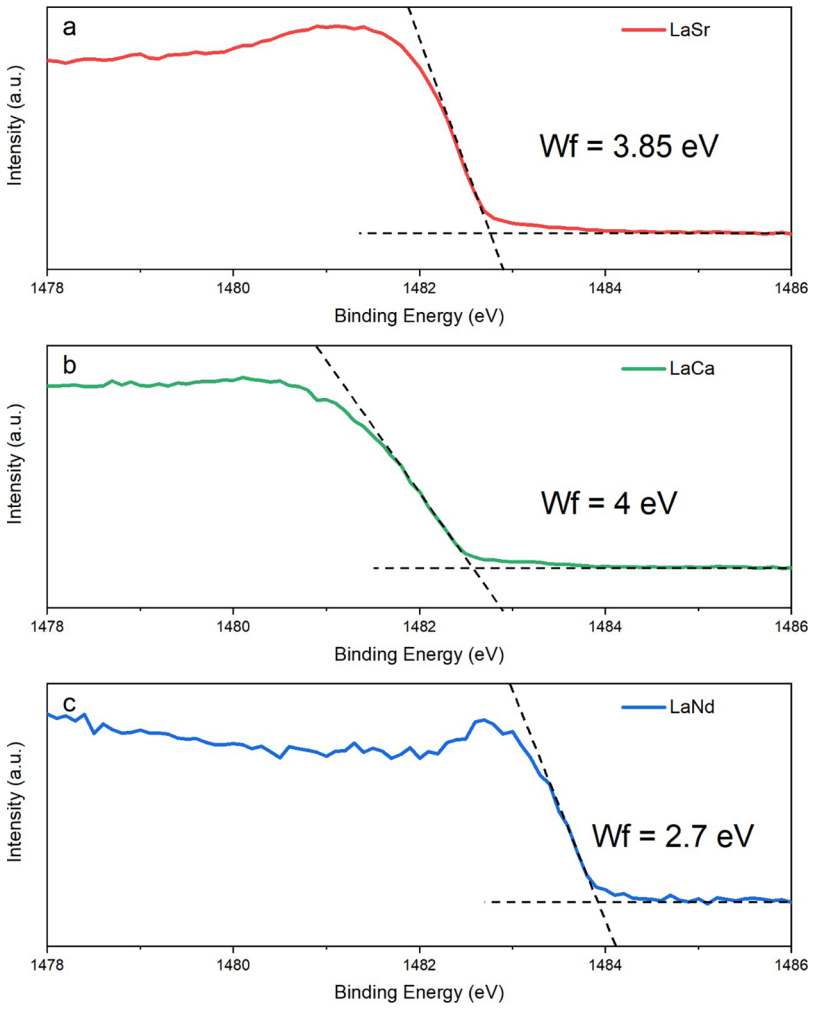

Figure 5. Work function (WF) values in eV for (c) LaNd, (b) LaCa, and (a) LaSr, respectively.

densities. K−L plots were derived from LSV measurements conducted at 400, 800, 1200, 1600, and 2000 rpm with a scan rate of 5 mV s^{-1} over a potential range of 1.2 V to 0.14 V vs. RHE. As the rotation speed increased, the reduction current rose due to enhanced mass transport at the electrode surface, with higher rpm enabling more efficient oxygen diffusion from the electrolyte to the catalyst.

The linearity of the K−L plots confirms that ORR follows first-order kinetics (Figure 7c).

The electron transfer number (n) calculated at 0.15 V vs. RHE was 2.44 for LaSr, 3.48 for LaNd, and 2.16 for LaCa (Figure 7d). These results suggest a mixed two- and four-electron pathway for LaSr and LaCa, while the ORR on LaNd is predominantly a four-electron process.

The bifunctional index (BI), determined from the potential difference between −1 and 10 mA cm^{-2}, indicates that lower BI values correspond to better OER and ORR performance. The BI values for LaSr, LaNd, and LaCa were 0.87, 1.03, and 1.02, respectively, showing that LaSr has a slightly better bifunctional performance.

OER/ORR performance metrics and bifunctional activity of recently reported electrocatalysts are included in the Supporting Information Table S1 for a comprehensive comparison of the electrocatalytic performance of the samples. Overall, LaNd emerges as the most promising OER electrocatalyst among A/HEPOs due to its low overpotential, small Tafel slope, and high intrinsic activity (MA and SA), as a result of its higher oxygen vacancy concentration and lower work function. Conversely, LaSr, with more positive onset and half-wave potentials and a relatively low BI, is better suited for ORR. Although LaCa exhibits comparable metrics, it cannot be considered a reliable bifunctional catalyst due to its multiphase nature. In summary, LaNd is highly effective for OER, while LaSr is more favorable for ORR, highlighting the effectiveness of A-site doping in tuning the bifunctional activity of HEPOs.

3.3. ZAB Performance

The performance of the A/HEPO electrocatalysts was assessed using a custom-built ZAB configuration. The setup includes a zinc plate as the anode, a 6 M potassium hydroxide (KOH) electrolyte containing 0.2 M zinc acetate ($Zn(OAc)_2$), and a carbon cloth cathode coated with the HEPO electrocatalyst.

The polarization curves illustrating the charge−discharge behavior of ZABs with A/HEPO air cathodes are shown in Figure 8a. At a current density of 10 mA cm^{-2}, the ZAB with a LaCa cathode requires 2.145 V for charging and 0.956 V for discharging. Although LaCa exhibits the highest peak power density with 81 mW cm^{-2} at 151 mA cm^{-2}, it is not a

https://doi.org/10.1021/acsaem.6c00383
ACS Appl. Energy Mater. 2026, 9, 6823−6835

Downloaded from pubs.acs.org/aaemcq/article-pdf/9/11/6823/6019466/ae-2026-00383e.pdf by ORTA DOGU TEKNIK UNIV user on 23 September 2026

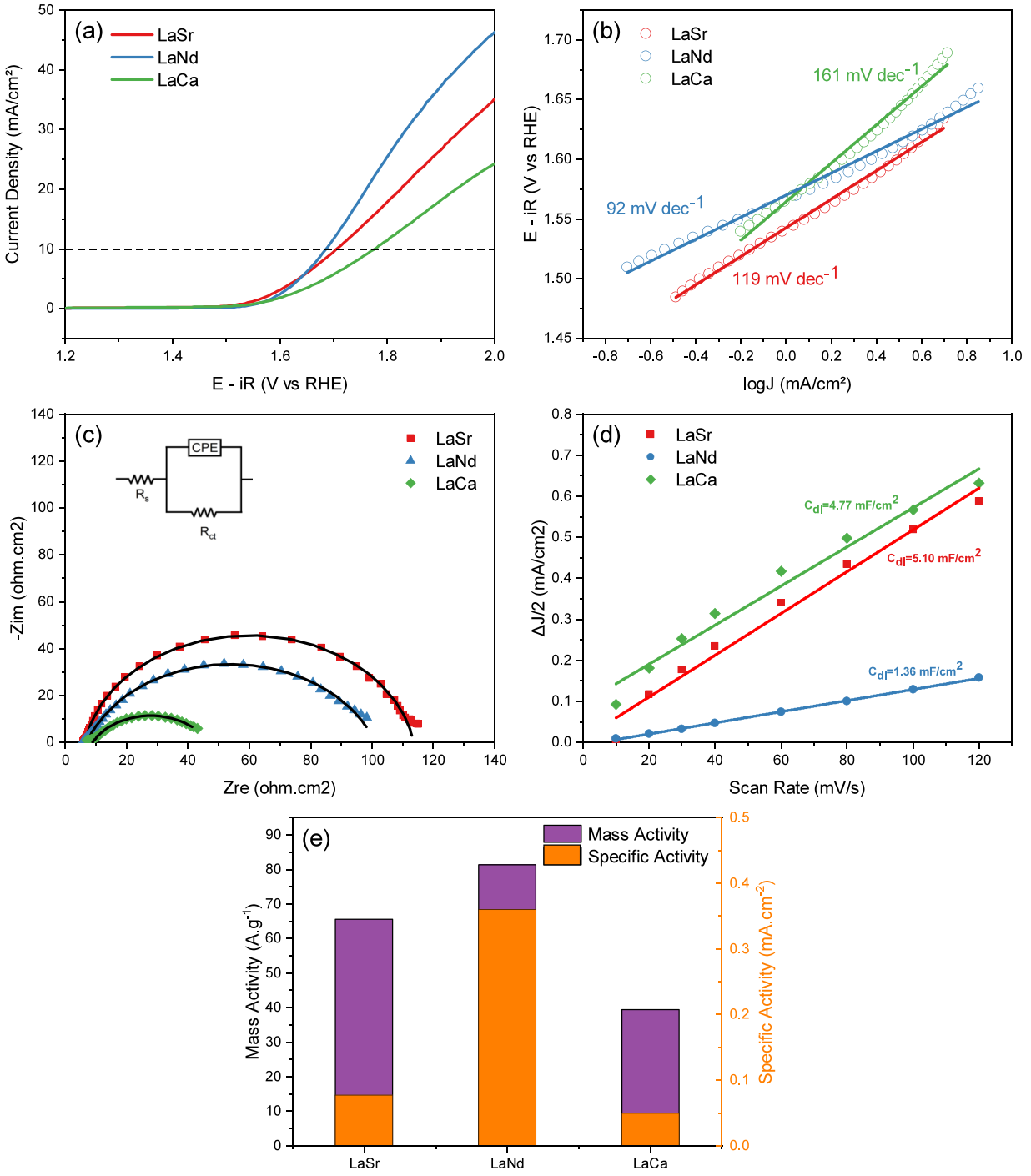

Figure 6. (a) OER activity curves of the A/HEPO samples (b) Tafel slopes obtained from the steady-state region (c) electrochemical impedance spectroscopy of the A/HEPOs at a potential of 1.641 V vs. RHE (d) electrical double-layer capacitance and (e) mass (MA) and specific activities (SA).

single-phase material, as indicated by XRD, and the presence of secondary phases may influence its apparent performance. ZABs with LaNd and LaSr cathodes have slightly lower peak power densities, 65 mW cm^{-2} at 127 mA cm^{-2} and 62 mW cm^{-2} at 119 mA cm^{-2}, respectively but provide more reliable indicators of intrinsic electrocatalytic performance, with comparable voltage windows.

The discharge capacities of ZABs using LaSr, LaNd, and LaCa A/HEPO cathodes were measured at current densities of 5, 10, and 20 mA cm^{-2}, and the results are presented in Figure 8b–d. As expected, the discharge capacities decrease with increasing current density from 5 to 20 mA cm^{-2}.

Specifically, the LaCa-cathode ZAB delivers capacities of 647.49 mA·h at 5 mA cm^{-2}, 525.07 mA·h at 10 mA cm^{-2}, and 424.88 mA·h at 20 mA cm^{-2}. Although the LaCa cathode achieves the highest capacity at 5 mA cm^{-2}, its capacity decreases more rapidly than those of LaNd and LaSr cathodes with increasing discharge current. Consequently, at 20 mA cm^{-2}, LaCa ranks

https://doi.org/10.1021/acsaem.6c00383
ACS Appl. Energy Mater. 2026, 9, 6823−6835

Downloaded from pubs.acs.org/aaemcq/article-pdf/9/11/6823/6019466/ae-2026-00383e.pdf by ORTA DOGU TEKNIK UNIV user on 23 September 2026

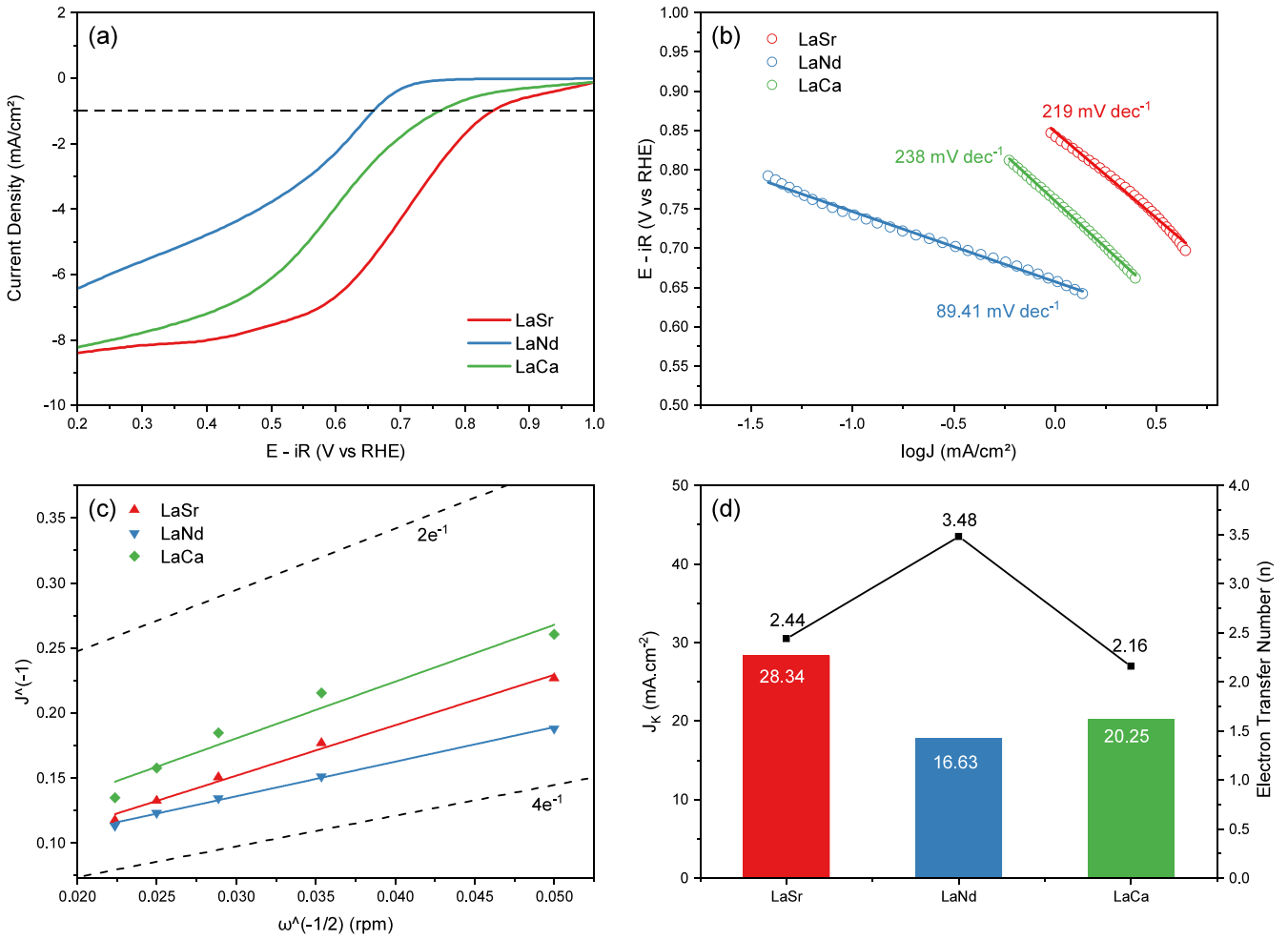

Figure 7. (a) ORR activity curves of A/HEPOs (b) Tafel plots of A/HEPOs obtained from the steady-state region (c) Koutecky–Levich plots at 0.15 V (d) kinetic current density (Jk) and number of electrons transferred (n) for A/HEPOs.

second among the A/HEPO electrocatalysts. The observed capacity decline in LaCa-based batteries can be attributed to the presence of oxide phases in the crystal structure, which reduce stability. In contrast, LaNd-based and LaSr-based ZABs maintain their capacities.

In particular, LaNd-based batteries exhibit capacities of 547.49 mA·h at 5 mA cm^{-2}, 463.67 mA·h at 10 mA cm^{-2}, and 435.38 mA·h at 20 mA cm^{-2}, showing more stable capacity retention and lower sensitivity to current density increases compared with LaCa and LaSr.

As shown in Figure 8e and the cycling stability and rate capability of ZABs with LaSr, LaNd, and LaCa A/HEPO electrocatalysts were systematically evaluated by increasing the discharge current from 0 to 20 mA cm^{-2} and then decreasing it back to 0 mA cm^{-2} while recording the output voltage. Among these A/HEPO-based ZABs, LaSr and LaCa electrocatalysts demonstrate the best rate capability. Initially, the output voltage for LaSr and LaCa was approximately 1.41 V, which decreased to 1.34 V after 400 min, retaining 95.04% of the initial voltage. By comparison, the LaNd-based ZAB started at 1.44 V and dropped to 1.29 V over the same period, indicating a higher voltage decay and a retention of 89.58%.

Figure 8f shows the cyclic charge–discharge performance of ZABs with LaSr, LaNd, and LaCa A/HEPO electrocatalysts. The performance was evaluated at a constant current density of 5 mA cm^{-2} using 5-minute charge–discharge cycles to assess the electrochemical durability of the catalysts. Initially, the LaNd-based ZAB exhibited charge and discharge voltages of 2.02 V and 1.04 V, respectively, resulting in a relatively small voltage gap of 962 mV. In contrast, the voltage gaps of LaSr-based and LaCa-based batteries were slightly larger at 1030 mV and 1010 mV, respectively (Figure 8f). Specifically, the LaSr-based battery initially showed 2.10 and 1.07 V, while the LaCa-based battery showed 2.06 and 1.05 V. This indicates that at the start of the cycling test, the LaNd-based battery had the smallest voltage gap. As the test progressed, the voltage gaps of LaSr-based and LaCa-based batteries increased, leaving the LaNd-based battery with the smallest voltage gap among the A/HEPO-based ZABs. After 300 h of operation, the LaSr-based battery began to lose stability, and the LaCa-based battery showed signs of instability after approximately 350 h. Notably, the LaNd-based ZAB maintained stability for over 450 h of cycling, showing only minimal increase in the voltage gap. At the end of this long-term test, the voltage gap of the LaNd-based ZAB increased by only 5.67% compared with the initial value, reaching 1020 mV after 450 h.

These results suggest that the strong OER activity of LaNd A/HEPO, due to its high oxygen vacancy content and low work

Downloaded from pubs.acs.org/aaemcq/article-pdf/9/11/6823/6019466/ae-2026-00383e.pdf by ORTA DOGU TEKNIK UNIV user on 23 September 2026

https://doi.org/10.1021/acsaem.6c00383
ACS Appl. Energy Mater. 2026, 9, 6823–6835

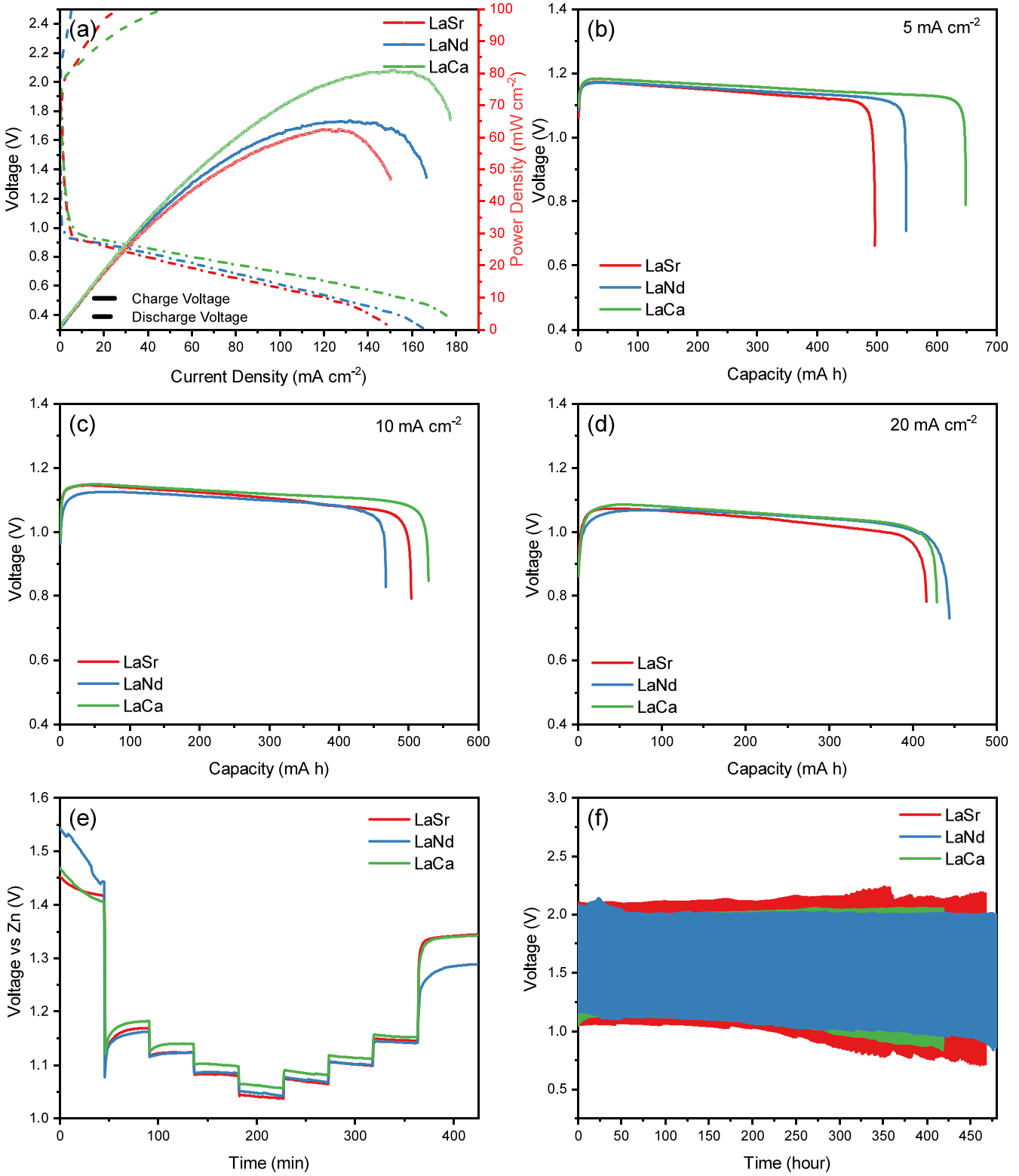

Figure 8. Zn–air batteries using A/HEPO electrocatalysts as the air cathode (a) charge–discharge polarization curves and the corresponding peak power density plots (b) capacities at a current density of 5 mA·cm^{-2} (c) capacities at 10 mA·cm^{-2} (d) capacities at 20 mA·cm^{-2} (e) rate capability test from 0 to 20 mA·cm^{-2} and back to 0 mA·cm^{-2} (f) cyclic charge–discharge stability at 5 mA·cm^{-2}.

function, likely contributes to the high performance and long-term stability observed in battery tests. Therefore, a direct correlation can be established between the electrocatalytic properties and battery behavior. LaSr-doped A/HEPO, with its low bifunctional index and high ORR activity, also performs well as a battery material; however, it does not provide as much

https://doi.org/10.1021/acsaem.6c00383
ACS Appl. Energy Mater. 2026, 9, 6823–6835

Downloaded from pubs.acs.org/aaemcq/article-pdf/9/11/6823/6019466/ae-2026-00383e.pdf by ORTA DOGU TEKNIK UNIV user on 23 September 2026

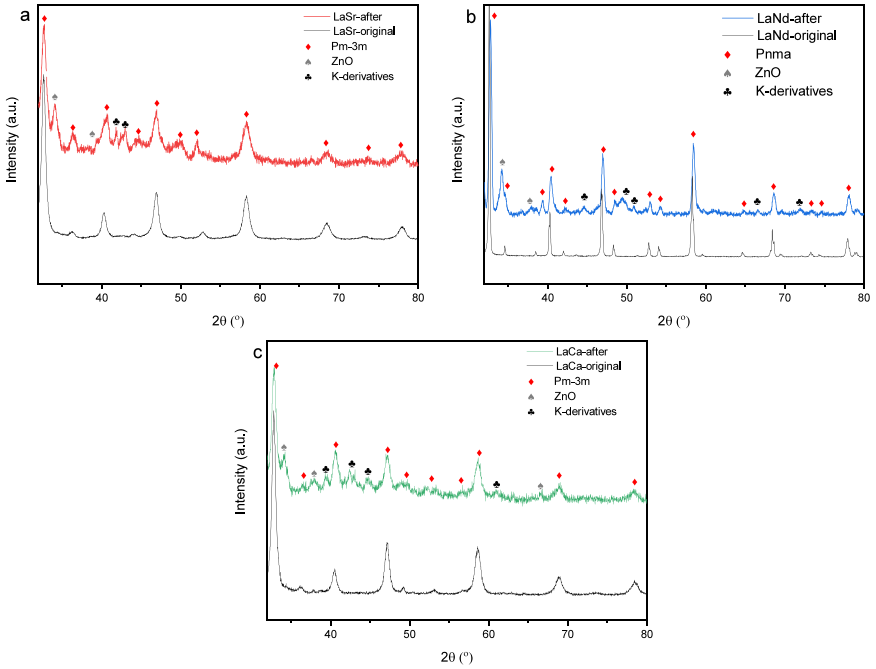

Figure 9. Comparison of pre-cycling and post-cycling XRD measurements of (a) LaSr, (b) LaNd, and (c) LaCa.

long-term stability as LaNd. Meanwhile, LaCa-doped HEPO delivers high initial capacity and power density but may experience performance losses over time due to phase instability associated with its multiphase structure.

3.4. Crystal Structure Characterization after Battery Test

Post-cycling XRD measurements (Figure 9) were performed to investigate phase evolution in the A-site modified HEPO catalysts after 450 h of operation. The spectra confirm the preservation of the primary perovskite phases (pm − 3m for LaSr/LaCa; Pnma for LaNd), indicating excellent structural stability. There is only a slight shift on the LaNd sample (Figure 9b) after prolonged cyclic charge-discharge experiment, which indicates the lattice contraction during the operation. Additional peaks associated with potassium derivatives (oxides/hydroxides) and zinc oxide (31.5° and $34.4°) were also detected. These secondary phases are attributed to the precipitation of electrolyte components (6 M KOH and $Zn(OAc)_2$) and potential zinc crossover on the carbon cloth substrate during the extensive immersion period, rather than degradation of the catalyst material itself. Consequently, it can be concluded that the crystal structure of the A/HEPOs remains stable throughout the prolonged 450-hour test.

■ CONCLUSIONS

In this study, single-phase, cubic perovskite-structured A-site−doped HEPOs were successfully synthesized. The electrocatalytic performance of the A/HEPOs was comprehensively evaluated. LaNd A/HEPO stood out particularly for OER, exhibiting an overpotential of 459 mV at a current density of 10 mA cm^{-2}. The improved OER activity was attributed to its increased oxygen vacancy content and optimized work function, which may cause high stability and long cycling life in ZABs. LaSr A/HEPO showed notable ORR performance, a high ORR activity with an onset potential of 0.84 V at −1 mA cm^{-2}; however, it did not demonstrate the same long-term durability as LaNd in extended cycling tests. For LaCa stability issues arose over time due to the inability to achieve a single-phase structure. These findings indicate that A-site doping is a critical strategy for directly influencing oxygen vacancy content and work function to enhance OER performance, and that LaNd A-site doped HEPO, in particular, provides superior ZAB performance through its high OER and comparable ORR activity.

■ ASSOCIATED CONTENT

Supporting Information

The Supporting Information is available free of charge at https://pubs.acs.org/doi/10.1021/acsaem.6c00383.

Super P carbon's electrochemical OER/ORR activity, LSV curves obtained from measurements performed with independently prepared catalyst inks, comparison of OER/ ORR performance and bifunctional activity of previously reported electrocatalysts, and BET analysis (DOCX)

■ AUTHOR INFORMATION

Corresponding Author

Cigdem Toparli – *Department of Metallurgical and Materials Engineering, Middle East Technical University, Ankara 06800, Türkiye; Energy Storage Materials and Devices Research Center (ENDAM), Middle East Technical University, Ankara 06800, Türkiye;* orcid.org/0000-0002-4374-4910; Email: ctoparli@metu.edu.tr

Authors

Cagla Ozgur – *Department of Metallurgical and Materials Engineering, Middle East Technical University, Ankara 06800, Türkiye*

Downloaded from pubs.acs.org/aaemcq/article-pdf/9/11/6823/6019466/ae-2026-00383e.pdf by ORTA DOGU TEKNIK UNIV user on 23 September 2026

https://doi.org/10.1021/acsaem.6c00383
ACS Appl. Energy Mater. 2026, 9, 6823−6835

Tuncay Erdil – *Department of Metallurgical and Materials Engineering, Middle East Technical University, Ankara 06800, Türkiye*; orcid.org/0000-0002-5187-5902
Uygar Geyikci – *Department of Metallurgical and Materials Engineering, Middle East Technical University, Ankara 06800, Türkiye*
Huseyin Inan Cihan – *Department of Metallurgical and Materials Engineering, Middle East Technical University, Ankara 06800, Türkiye*
Ilker Yildiz – *Central Laboratory, Middle East Technical University, Ankara 06800, Türkiye*; orcid.org/0000-0001-5761-655X

Complete contact information is available at: https://pubs.acs.org/doi/10.1021/acsaem.6c00383

Author Contributions

‡C.O. and T.E. contributed equally. The manuscript was written through the contributions of all authors. All authors have given approval to the final version of the manuscript.

Funding

This work was financially supported by the Middle East Technical University Scientific Research Projects Coordination Unit under grant number "ADEP-308-2023-11194" and "GAP-801-2025-11546".

Notes

The authors declare no competing financial interest.

REFERENCES

(1) Zhou, C.; Chen, X.; Liu, S.; Han, Y.; Meng, H.; Jiang, Q.; Zhao, S.; Wei, F.; Sun, J.; Tan, T.; Zhang, R. Superdurable Bifunctional Oxygen Electrocatalyst for High-Performance Zinc−Air Batteries. *J. Am. Chem. Soc.* **2022**, *144* (6), 2694–2704.
(2) Li, Y.; Gong, M.; Liang, Y.; Feng, J.; Kim, J. E.; Wang, H.; Hong, G.; Zhang, B.; Dai, H. Advanced Zinc-Air Batteries Based on High-Performance Hybrid Electrocatalysts. *Nat. Commun.* **2013**, *4* (1), 1805.
(3) Deng, Y. P.; Jiang, Y.; Liang, R.; Zhang, S. J.; Luo, D.; Hu, Y.; Wang, X.; Li, J. T.; Yu, A.; Chen, Z. Dynamic Electrocatalyst with Current-Driven Oxyhydroxide Shell for Rechargeable Zinc-Air Battery. *Nat. Commun.* **2020**, *11* (1), No. 1952.
(4) Leong, K. W.; Wang, Y.; Ni, M.; Pan, W.; Luo, S.; Leung, D. Y. C. Rechargeable Zn-Air Batteries: Recent Trends and Future Perspectives. *Renew. Sustain. Energy Rev.* **2022**, *154*, No. 111771.
(5) Hopkins, B. J.; Chervin, C. N.; Long, J. W.; Rolison, D. R.; Parker, J. F. Projecting the Specific Energy of Rechargeable Zinc−Air Batteries. *ACS Energy Lett.* **2020**, *5* (11), 3405–3408.
(6) Deng, Y. P.; Liang, R.; Jiang, G.; Jiang, Y.; Yu, A.; Chen, Z. The Current State of Aqueous Zn-Based Rechargeable Batteries. *ACS Energy Lett.* **2020**, *5* (5), 1665–1675.
(7) Fu, J.; Cano, Z. P.; Park, M. G.; Yu, A.; Fowler, M.; Chen, Z. Electrically Rechargeable Zinc−Air Batteries: Progress, Challenges, and Perspectives. *Adv. Mater.* **2017**, *29* (7), No. 1604685.
(8) Fu, J.; Liang, R.; Liu, G.; Yu, A.; Bai, Z.; Yang, L.; Chen, Z. Recent Progress in Electrically Rechargeable Zinc−Air Batteries. *Adv. Mater.* **2019**, *31* (31), No. 1805230.
(9) Lee, S.; Choi, J.; Kim, M.; Park, J.; Park, M.; Cho, J. Material Design and Surface Chemistry for Advanced Rechargeable Zinc-Air Batteries. *Chem Sci.* **2022**No. 136159.
(10) Wang, X. X.; Yang, X.; Liu, H.; Han, T.; Hu, J.; Li, H.; Wu, G. Air Electrodes for Flexible and Rechargeable Zn−Air Batteries. *Small Struct.* **2022**, *3* (1), No. 2100103.
(11) Cherevko, S.; Geiger, S.; Kasian, O.; Kulyk, N.; Grote, J. P.; Savan, A.; Shrestha, B. R.; Merzlikin, S.; Breitbach, B.; Ludwig, A.; Mayrhofer, K. J. J. Oxygen and Hydrogen Evolution Reactions on Ru, RuO_2, Ir, and IrO_2 Thin Film Electrodes in Acidic and Alkaline Electrolytes: A Comparative Study on Activity and Stability. *Catal. Today* **2016**, *262*, 170–180.
(12) Wei, C.; Rao, R. R.; Peng, J.; Huang, B.; Stephens, I. E. L.; Risch, M.; Xu, Z. J.; Shao-Horn, Y. Recommended Practices and Benchmark Activity for Hydrogen and Oxygen Electrocatalysis in Water Splitting and Fuel Cells. *Adv. Mater.* **2019**, *31* (31), No. 1806296.
(13) Wang, S.; Lu, A.; Zhong, C. J. Hydrogen Production from Water Electrolysis: Role of Catalysts. *Nano Converg.* **2021**, *8* (1), 4.
(14) Maiyalagan, T.; Jarvis, K. A.; Therese, S.; Ferreira, P. J.; Manthiram, A. Spinel-Type Lithium Cobalt Oxide as a Bifunctional Electrocatalyst for the Oxygen Evolution and Oxygen Reduction Reactions. *Nat. Commun.* **2014**, *5* (1), 3949.
(15) McCrory, C. C. L.; Jung, S.; Peters, J. C.; Jaramillo, T. F. Benchmarking Heterogeneous Electrocatalysts for the Oxygen Evolution Reaction. *J. Am. Chem. Soc.* **2013**, *135* (45), 16977–16987.
(16) Tong, Y.; Wu, J.; Chen, P.; Liu, H.; Chu, W.; Wu, C.; Xie, Y. Vibronic Superexchange in Double Perovskite Electrocatalyst for Efficient Electrocatalytic Oxygen Evolution. *J. Am. Chem. Soc.* **2018**, *140* (36), 11165–11169.
(17) Erdil, T.; Toparli, C. B-Site Effect on High-Entropy Perovskite Oxide as a Bifunctional Electrocatalyst for Rechargeable Zinc−Air Batteries. *ACS Appl. Energy Mater.* **2023**, *6* (21), 11255–11267.
(18) Erdil, T.; Ozgur, C.; Geyikci, U.; Lokcu, E.; Toparli, C. Earth-Abundant Divalent Cation High-Entropy Spinel Ferrites as Bifunctional Electrocatalysts for Oxygen Evolution and Reduction Reactions. *ACS Appl. Energy Mater.* **2024**, *7* (18), 7775–7786.
(19) Song, J.; Chen, Y.; Huang, H.; Wang, J.; Huang, S. C.; Liao, Y. F.; Fetohi, A. E.; Hu, F.; Chen, H. yi; Li, L.; Han, X.; El-Khatib, K. M.; Peng, S. Heterointerface Engineering of Hierarchically Assembling Layered Double Hydroxides on Cobalt Selenide as Efficient Trifunctional Electrocatalysts for Water Splitting and Zinc-Air Battery. *Adv. Sci.* **2022**, *9* (6), No. 2104522.
(20) Anand, P.; Wong, M. S.; Fu, Y. P. Perovskite Oxide Composites for Bifunctional Oxygen Electrocatalytic Activity and Zinc-Air Battery Application- a Mini-Review. *Energy Storage Mater.* **2023**, *58*, 362–380.
(21) Ali, Y.; Dwivedi, S.; Alivand, M. S.; Sanjid, A.; Tanksale, A.; Chakraborty Banerjee, P. Highly Stable and Porous Triple Perovskite Oxide as a Bifunctional Electrocatalyst for Rechargeable Zn-Air Batteries. *Chem. Eng. J.* **2025**, *516*, No. 163928.
(22) Riquelme-García, P.; García-Rodríguez, M.; Flores-Lasluisa, J. X.; Cazorla-Amorós, D.; Morallón, E. Enhanced Electrocatalytic Performance of $SrMn_{1-x}Co_xO_3$ Perovskite Metal Oxides for Oxygen Reactions in Zn-Air Batteries: Influence of Mn/Co Ratio. *Appl. Surf. Sci. Adv.* **2025**, *27*, No. 100725.
(23) Li, K.; Li, Y.; Han, X.; Shao, Q.; Lü, Z. Quenching-Induced Surface Reconstruction of Perovskite Oxides Activating Bifunctional Sites towards Oxygen Electrodes for Recharge Zinc−Air Batteries. *Energy Storage Mater.* **2025**, *78*, No. 104289.
(24) Christy, M.; Choi, S.; Kwon, J.; Jeong, J.; Paik, U.; Song, T. The Perfect Imperfections of Perovskite Oxide Catalysts in the Aspect of Defect Equilibria. *Small Sci.* **2025**, *5* (1), No. 2400386.
(25) Dai, Y.; Yu, J.; Cheng, C.; Tan, P.; Ni, M. Mini-Review of Perovskite Oxides as Oxygen Electrocatalysts for Rechargeable Zinc−Air Batteries. *Chem. Eng. J.* **2020**, *397*, No. 125516.
(26) Shen, Z.; Qu, M.; Shi, J.; Oropeza, F. E.; Peña O'Shea, V. A.de la; Gorni, G.; Tian, C. M.; Hofmann, J. P.; Cheng, J.; Li, J.; Zhang, K. H. L. Correlating the Electronic Structure of Perovskite $La_{1-x}Sr_xCoO_3$ with Activity for the Oxygen Evolution Reaction: The Critical Role of Co 3d Hole State. *J. Energy Chem.* **2022**, *65*, 637–645.
(27) Zhu, Y.; Zhou, W.; Yu, J.; Chen, Y.; Liu, M.; Shao, Z. Enhancing Electrocatalytic Activity of Perovskite Oxides by Tuning Cation Deficiency for Oxygen Reduction and Evolution Reactions. *Chem. Mater.* **2016**, *28* (6), 1691–1697.

Downloaded from pubs.acs.org/aaemcq/article-pdf/9/11/6823/6601946/ae-2026-00383e.pdf by ORTA DOGU TEKNIK UNIV user on 23 September 2026

(28) Liu, Z.; Tang, Z.; Song, Y.; Yang, G.; Qian, W.; Yang, M.; Zhu, Y.; Ran, R.; Wang, W.; Zhou, W.; Shao, Z. High-Entropy Perovskite Oxide: A New Opportunity for Developing Highly Active and Durable Air Electrode for Reversible Protonic Ceramic Electrochemical Cells. *Nano-Micro Lett.* **2022**, *14* (1), 217.
(29) Ji, X.; Yang, F.; Du, Y.; Li, J.; Li, J.; Hu, Q. Highly Active and Durable $La_{0.6}Ca_{0.4}(CrMnFeCo_2Ni)O_3$ High Entropy Perovskite Oxide as Electrocatalyst for Oxygen Evolution Reaction in Alkaline Media. *J. Mater. Sci. Technol.* **2024**, *168*, 71–78.
(30) Xu, X.; Pan, Y.; Ge, L.; Chen, Y.; Mao, X.; Guan, D.; Li, M.; Zhong, Y.; Hu, Z.; Peterson, V. K.; Saunders, M.; Chen, C. T. e; Zhang, H.; Ran, R.; Du, A.; Wang, H.; Jiang, S. P.; Zhou, W.; Shao, Z. High-Performance Perovskite Composite Electrocatalysts Enabled by Controllable Interface Engineering. *Small* **2021**, *17* (29), No. 2101573.
(31) Yan, X.; Zhou, Y.; Wang, S. Nano-High Entropy Materials in Electrocatalysis. *Adv. Funct. Mater.* **2025**, *35* (2), No. 2413115.
(32) Qiu, Z.; Guo, X.; Cao, S.; Du, M.; Wang, Q.; Pi, Y.; Pang, H. High-Entropy Ag−Ru-Based Electrocatalysts with Dual-Active-Center for Highly Stable Ultra-Low-Temperature Zinc-Air Batteries. *Angew. Chem., Int. Ed.* **2025**, *64* (3), No. e202415216.
(33) Gu, T.; Zhang, C.; Xi, L.; Ouyang, L.; Zhu, M.; Liu, J. High-Entropy Electrocatalytic Materials in Zn-Air Batteries: From Fundamentals to Applications. *Adv. Mater.* **2025**No. e12274.
(34) Sun, J.; Liu, W.; Liang, F.; Liu, R.; Yao, Y.; Zou, Q.; Dong, P.; Wang, S. Insight Into High Entropy Compounds: Advances, Challenges and Energy Applications. *Adv. Funct. Mater.* **2025**No. e10855.
(35) Sen, S.; Kumar, A.; Sharma, A. K.; Mandal, T. K. Unraveling e G-Band Modulation as an Alternative Strategy to Enhance Lattice Oxygen Participation and Oxygen Electrocatalytic Bifunctionality via Switching the Active Site. *J. Mater. Chem.y A* **2025**, *13*, 17075.
(36) Nguyen, T. X.; Liao, Y. C.; Lin, C. C.; Su, Y. H.; Ting, J. M. Advanced High Entropy Perovskite Oxide Electrocatalyst for Oxygen Evolution Reaction. *Adv. Funct. Mater.* **2021**, *31* (27), No. 2101632.
(37) Song, J.; Wei, C.; Huang, Z.-F.; Liu, C.; Zeng, L.; Wang, X.; Xu, Z. J. A Review on Fundamentals for Designing Oxygen Evolution Electrocatalysts. *Chem. Soc. Rev.* **2020**, *49*, No. 2196.
(38) Rong, X.; Parolin, J.; Kolpak, A. M. A Fundamental Relationship between Reaction Mechanism and Stability in Metal Oxide Catalysts for Oxygen Evolution. *ACS Catal.* **2016**, *6* (2), 1153–1158.
(39) Geng, H.; Zou, X.; Min, Y.; Bu, Y.; Lu, Q.; Geng, H.; Min, Y.; Bu, Y.; Lu, Q.; Zou, X. Advances and Challenges in Perovskite Oxide Design for High-Performance Zinc−Air Batteries: Integrating Experimental Strategies and Machine Learning. *Adv. Funct. Mater.* **2025**, *35* (32), No. 2500657.
(40) Yang, X.; Le, F.; Shu, W.; Cao, X.; Jia, W. Rational Electronic Regulation and Surface Reconstruction in Fe-Doped $La_{0.5}$ $Ba_{0.5}$ $CoO_{3-\delta}$ Perovskite for High-Current-Density Hydrogen Evolution Reaction and Efficient Oxygen Evolution Reaction. *Adv. Funct. Mater.* **2025**.
(41) Wei, C.; Sun, S.; Mandler, D.; Wang, X.; Qiao, S. Z.; Xu, Z. J. Approaches for Measuring the Surface Areas of Metal Oxide Electrocatalysts for Determining Their Intrinsic Electrocatalytic Activity. *Chem. Soc. Rev.* **2019**, *48* (9), 2518–2534.
(42) Tian, C.; Wang, D.; Zhang, K. H. L.; Hofmann, J. P. Evaluating the Effect of Oxygen Vacancies on the Oxygen Evolution Reaction (OER) Activity of $LaNiO_3$. *Langmuir* **2025**, *41* (13), 8565–8573.
(43) Sunding, M. F.; Hadidi, K.; Diplas, S.; Løvvik, O. M.; Norby, T. E.; Gunnæs, A. E. XPS Characterisation of in Situ Treated Lanthanum Oxide and Hydroxide Using Tailored Charge Referencing and Peak Fitting Procedures. *J. Electron Spectrosc. Relat. Phenom.* **2011**, *184* (7), 399–409.
(44) Nasser, S.; Cohen-Taguri, G.; Mass, T.; Pinkas, I.; Goobes, G. Analysis of $Ca_{1-X}Sr_xCO_3$ Phases Generated by Competitive Sr^{2+} Replacement in Pre-Formed Aragonite. *Heliyon* **2024**, *10* (17), No. e36648.

Downloaded from pubs.acs.org/aaemcq/article-pdf/9/11/6823/6019466/ae-2026-00383e.pdf by ORTA DOGU TEKNIK UNIV user on 23 September 2026

https://doi.org/10.1021/acsaem.6c00383
ACS Appl. Energy Mater. 2026, 9, 6823−6835